COUPLED STEAM AND THERMAL GRADIENT EFFECTS ON EBCs

Matthew Caulfield, Dr. Elizabeth Opila (Advisor)
University of Virginia
Virginia Space Grant Consortium 2025 Student Research Conference

Abstract

Ytterbium disilicate ($Yb_2Si_2O_7$, YbDS) has emerged as a key environmental barrier coating (EBC) material for protecting silicon carbide (SiC)-base ceramic matrix composites (CMCs) in gas turbine engines, where high-temperature, high-velocity steam drives silica loss and phase transformation. This work quantified silica depletion and the transformation of YbDS to form an ytterbium monosilicate (Yb_2SiO_5, YbMS) reaction layer, using a custom-built horizontal "steam jet" furnace capable of producing ~250 m/s water vapor at temperatures up to 1500 °C. Results for both sintered and atmospheric plasma sprayed (APS) material are compared. Building on this, coupled high-temperature, high-velocity steam exposure and thermal gradient tests were conducted to assess how increasing YbMS layer depth of formation promotes crack initiation and propagation across coating interfaces.

Introduction

State of the art turbine blades are made of Ni-base superalloys with thermal barrier coatings, which are currently operating near their melting temperature on existing aircraft engines. The drive for higher engine operating temperatures creates a critical need to identify and test alternative materials that can withstand these greater temperatures. SiC-based CMCs offer a promising solution due to their high-temperature stability, strength, and reduced weight (3× less dense than current Ni-base alloys) [1][2]. However, SiC-based CMCs suffer from environmental durability issues in high-temperature steam, generated by the combustion of jet fuel, and molten deposits resulting from the ingestion of calcium magnesium alumino-silicate (CMAS) found in sand and volcanic ash. These environments can degrade the performance of the SiC-based CMC and lead to a loss of the material over time.

Therefore, EBCs are essential to protect CMCs. They are applied on top of the CMC as a surface protective layer to protect the underlying structural components against high-temperature, high-velocity water vapor attack and degradation caused by CMAS. YbDS stands out as a state-of-the-art EBC material. The YbDS is distinctive as it has a CTE similar to the SiC-base CMC substrate, and is chemically compatible with the SiC-base CMC substrate. Upon exposure, a porous YbMS surface layer forms due to YbDS interaction with the high-temperature, high-velocity as seen in Equation (1) and Figure 1 [3].

$$Yb_2Si_2O_7(s) + 2H_2O(g) \rightarrow Yb_2SiO_5 + Si(OH)_4(g) \quad (1)$$

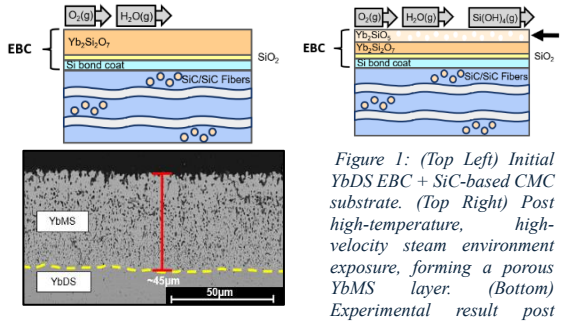

Figure 1: (Top Left) Initial YbDS EBC + SiC-based CMC substrate. (Top Right) Post high-temperature, high-velocity steam environment exposure, forming a porous YbMS layer. (Bottom) Experimental result post Steam exposure: t = 96 h, T = 1375°C

Although the reaction occurs, its reaction rate is comparatively lower when compared to the reactivity of SiC or SiO_2 when exposed to water vapor as seen in Figure 2.

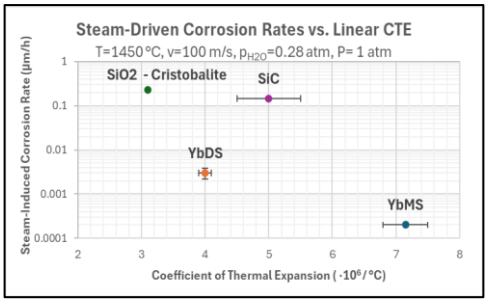

Figure 2: Corrosion rates of YbDS YbMS, SiO_2, and SiC, data collected from [4] and CTE data collected from [5][6]

Experimental Modeling – Steam

Approaches that combine microstructural characterization, reaction kinetics, and thermomechanical modeling are needed to accurately describe the evolution of EBCs in service, inform life predicting models, and strategies for enhanced durability of next generation coatings.

Previous iterations of high-temperature, high-velocity steam jet testing setups as seen in Figure 3 were limited by small sample sizes (~10 mm x 10 mm) and the incomplete vaporization of injected water, which allowed liquid droplets to impinge on the sample surface and cause mechanical erosion at the steam impingement site. These limitations not only restricted the area of coating exposed to high-temperature steam but also made it difficult to isolate purely thermochemical degradation processes from mechanical damage caused by droplet impacts [7].

To address these limitations, a new steam jet experimental setup was built and modified to increase the diameter of the steam-affected depletion region from ~5 mm to 25.4 mm. Expanding the steam impingement area enables the formation of a widespread reaction layer across a larger portion of the coating surface, providing sufficient degraded material for microstructural analysis and subsequent thermal gradient cycling experiments.

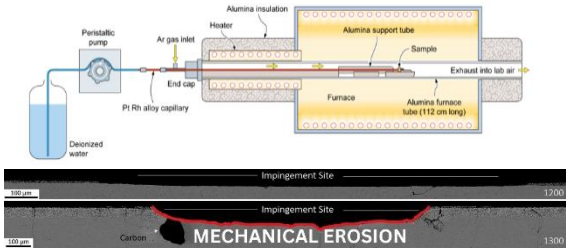

Figure 3: (Top) Technical illustration of previous design iteration of a high-temperature, high-velocity "steam jet" experimental setup. (Bottom) Experimental results of YbDS post 250 h exposure, demonstrating mechanical erosion of coating surface. [7]

Computational fluid dynamics (CFD) simulations were performed in ANSYS Fluent to characterize the flow of the high-velocity steam jet and to guide the experimental design. To explore the interactions between the steam jet and the sample surface, key variables were evaluated as seen in Figure 4, including: (1) sample angle, angle of incidence between the capillary tube and the sample surface (2) standoff distance, distance between the capillary tube exit and the sample surface (3) mass flow rate, volume of water delivered to the sample per unit time, and (4) capillary tube inner diameter, cross-sectional area of the capillary tube for steam transfer.

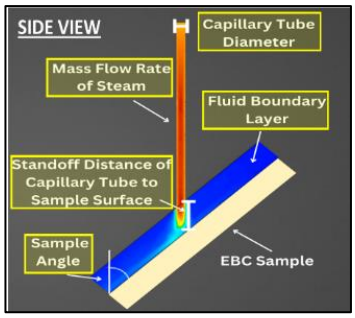

Figure 4: ANSYS Fluent side view profile of simulation setup for isolated variable analysis

The 45° sample angle was selected because it produced the largest steam impingement site, maximizing the area of coating exposed to high-velocity steam compared to 30° or 90° orientations. The standoff distance was set to 1 mm as shorter distances helped to maintain a greater steam jet velocity acting at the sample surface. Distances shorter than 1 mm were deemed difficult to repeat, limited steam impingement site size, and produced a highly localized jet acting on the sample. The mass flow rate was set to 1 mL/min to provide focused steam flow while eliminating droplet formation and decreasing saturation. Higher flow rates were found to introduce turbulence and mechanical erosion. Finally, a 1 mm capillary tube diameter was chosen to maintain a high exit velocity and minimize cost for experimental setup.

Table 1: ANSYS Fluent isolated variable study summary of results and selected design criteria to use in the experimental setup to increase steam impingement site size

Parameter	Values Tested	Selected Criteria to Use in Experimental Setup
Sample Angle	30°, 45°, 90°	45°
Standoff Distance	1 mm, 2 mm, 3 mm	1mm
Mass Flow Rate	1, 3, 9 mL/min	1 mL/min
Capillary Tube Inner Diameter	1 mm, 2 mm, 3 mm	1mm

In addition to the CFD simulations performed in ANSYS Fluent, analytical calculations were used to estimate and validate the theoretical steam jet velocity of the experimental setup. The following operating conditions were chosen to match the experimental model: T = 1375 °C, P = 1atm, $\dot{m}$ = 1 mL/min, D = 1 mm, M = 18.015 g/mol, and R= 8.314 J/mol*K. These calculations provide an of steam density (ρ_{Steam}) at temperature, viscosity of steam at temperature ($\mu_{1648.15K}$), average velocity of steam (V_{Avg}), and Reynolds number of steam (Re) at the capillary tube exit [8].

Sutherland's formula is used to estimate the steam viscosity at elevated temperatures. For this calculation, the Sutherland constant for steam (S_μ) is equal to 1064 K, the reference viscosity of steam (μ_{ref}) is equal to 1.12 * 10^{-5} Pa*s, and the reference temperature for steam (T_{ref}) is equal to 350 K [9][10].

$$\rho_{Steam} = \frac{PM}{RT} \quad (2)$$

$$\mu_{1648.15K} = \mu_{ref}\left(\frac{T}{T_{ref}}\right)^{\frac{3}{2}}\left(\frac{T_{ref}+S_\mu}{T+S_\mu}\right) \quad (3)$$

$$V_{Avg} = \frac{\dot{m}}{\rho_{Steam}A} \quad (4)$$

$$Re_{Avg} = \frac{\rho V_{Avg} D}{\mu_{1673.15K}} \quad (5)$$

$$V_{laminar\ centerline\ velocity} = 2V_{Avg} \quad (6)$$

Using the equations stated, $\mu_{1648.15K}$ was solved to be equal to 6x10^{-5} Pa*s, V_{Avg} was solved to be equal to 159 m/s, Re_{Avg} was solved to be equal to 356 (representing a laminar flow), and $V_{laminar\ centerline\ velocity}$ was solved to be equal to 319 m/s.

The calculated steam jet velocities fall within the same order of magnitude as gas velocities encountered by environmental barrier coatings in turbine engines, where combustion gas velocities typically range from 100–600 m/s depending on location in the engine and operating conditions [11][12]. As a result, the steam jet system provides a representative environment capable of reproducing the aggressive thermochemical degradation conditions experienced by EBC materials in service.

Experimental Setup – Steam

Steam exposure testing was performed using a modified high-temperature, high-velocity steam jet setup as seen in Figure 5 and is designed to simulate the aggressive high-temperature, high-velocity water vapor environments experienced by EBCs in turbine engine systems. The experimental setup was adapted from the steam jet design originally developed by dos Santos e Lucato at Teledyne Scientific and further modified at UVA to increase the diameter of the steam-affected depletion region and eliminate water droplet mechanical surface erosion [13].

In this system, deionized (DI) water was used as the steam source and delivered at a controlled mass flow rate using a peristaltic pump. The pump provided a constant rate of 1 mL/min, which was selected based on the CFD analysis described. Within the preheater, the water is directed toward the lower portion of the chamber and away from the capillary tube inlet. This setup allows for the water to fully vaporize and rise in the chamber before entering the capillary tube and furnace region for sample steam impingement. Following the preheater, the vaporized steam enters a choked flow region where the flow is constricted from a 3.175mm inner diameter Ni 200 tube to a 1 mm inner diameter platinum–rhodium (Pt/Rh) capillary

tube. This reduction in cross-sectional area accelerates the steam and promotes the formation of a high-velocity steam jet prior to steam impingement on the sample surface.

At this location in the system, both a pressure gauge and in-line thermocouple were incorporated into the modified design to allow direct monitoring of the steam condition prior to entering the capillary tube and horizontal tube furnace.

As the steam moves from the 700 °C preheating chamber, it continues to heat until reaching the furnace operating temperature of 1375 °C. The capillary tube was oriented at a 45° angle relative to the sample surface, with a 1 mm standoff distance, as determined from CFD analysis. Under these conditions, the steam exits the PtRh capillary tube inside the furnace at a high velocity estimated to be ~350 m/s and impinges on the coating surface, producing a localized region of elevated temperature and high-water vapor flux on the material surface.

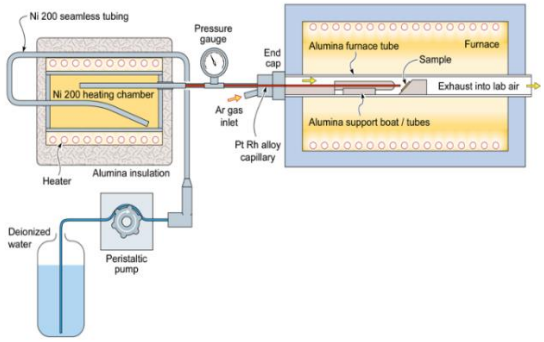

Figure 5: Technical illustration of modified high-temperature, high-velocity steam jet testing setup to increase the diameter of the steam-affected depletion region and reduce water droplet mechanical surface erosion

Sintered YbDS coupons and atmospheric plasma sprayed (APS) YbDS coatings were evaluated to assess the influence of initial microstructure on steam-induced reaction layer formation.

The sintered YbDS sample was fabricated from commercial YbDS powder through a powder processing and pelletization procedure designed to produce a dense bulk coupon. The powder was first horizontally ball milled for 24 h with zirconia milling media to improve powder homogeneity and reduce particle agglomeration. The milled powder was then mixed with 1mL of 2 wt% polyvinyl alcohol (PVA) in water binder to aid compaction and cold pressed in a 25.4 mm diameter die under 5 metric tons of pressure to form a green pellet. Following pressing, the pellet underwent binder burnout and sintering in a high-temperature box furnace using a heating profile consisting of a ramp rate to 500 °C for binder removal followed by sintering at 1500 °C to achieve coupon densification. This process produced a dense bulk YbDS sample with relatively isotropic microstructures compared to the lamellar, splat-based microstructure characteristic of APS coatings. The YbDS APS coating used for comparison was provided by Rolls-Royce. The APS coating was 25.4 mm diameter with a SiC-based CMC substrate.

Key differences between the samples arise from the synthesis process. The APS coating has a rougher surface compared to the sintered sample due to the splat-based nature of APS processing, where molten particles impact the substrate surface and rapidly solidify to form a layered microstructure. In addition, small amounts of YbMS are present in the nominal YbDS APS coating. This occurs during plasma spraying because some SiO_2 is lost in the high-temperature plasma plume, creating localized formation of the monosilicate phase. This results in a mixed-phase microstructure in the as-deposited APS coating compared to the sintered sample.

Following 96 h steam jet exposure, each sample was sputter coated with Au/Pd to prevent sample charging during electron imaging. A scanning electron microscope (SEM; FEI Quanta 650 FEG), was used to evaluate the microstructure of the coating system. Energy dispersive x-ray spectroscopy (EDS; Aztec X-MaxN 150) characterization was subsequently performed to

determine the elemental composition of the phases present within the coating system.

Samples were cross-sectioned using a low-speed saw through the center of the steam impingement region to capture the location of the maximum YbMS layer depth and spatial depth of formation change across the sample surface. SEM concentric backscatter (CBS) imaging confirmed phase change and EDS confirmed presence of the silica loss and monosilicate phase formation. Both horizontal and vertical cross-sections of the sample were performed, with steam flow moving from the bottom of the sample to the top of the sample shown in Figure 6. The horizontal direction cross-section runs perpendicular to the steam flow and enables the characterization of the reaction layer thickness and penetration depth across of the steam impingement site. The vertical-direction cross-section runs parallel to the steam flow and enables the characterization upstream and downstream of the steam impingement site.

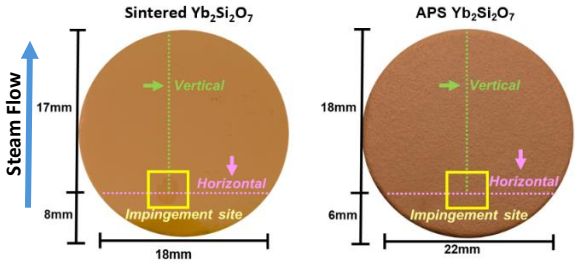

Figure 6: (Left) 1in Sintered YbDS sample with identified horizontal and vertical cross-sections. (Right) 1in APS YbDS sample with identified horizontal and vertical cross-sections

The prepared cross-sections were mounted in slow cure epoxy and polished to produce smooth surfaces suitable for high-resolution microscopy and compositional analysis. Samples were progressively ground using SiC paper of increasing grit size, followed by diamond polishing down to 0.25µm remove surface damage introduced during the sectioning and grinding process.

Following polishing, cross-sectional SEM imaging was conducted to characterize the thickness, morphology, and continuity of the steam-induced YbMS reaction layer across the coating system.

Results – Steam

All YbMS depth values were averaged across spatial areas of interest on the coating sample surface and labeled on the micrograph, representative of the average depth of YbMS formation in that region.

The sintered YbDS vertical cross-section sample as seen in Figure 7 measured 17 mm in length. SEM imaging revealed that the YbMS layer thickness gradually decreased from approximately 45 µm at the center of the steam impingement region to 25 µm near the edges of the cross-section.

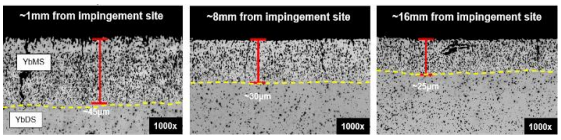

Figure 7: Sintered YbDS Vertical Cross-Section (Steam exposure: t = 96 h, T = 1375 ℃)

The APS YbDS horizontal cross-section sample as seen in Figure 8 measured 18 mm in length. SEM imaging revealed that the YbMS layer thickness gradually decreased from approximately 45 µm at the center of the steam impingement region to 20 µm near the edges of the cross-section.

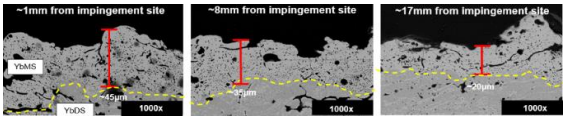

Figure 8: APS YbDS Vertical Cross-Section (Steam exposure: t = 96 h, T = 1375 ℃)

Using the SEM characterization results, a formation depth profile of the YbMS layer was constructed to map the spatial variation in monosilicate reaction depth across the sample surface as seen in Figure 9. Based on the measured cross-sections, the profile was divided into four regions:

Region 1: YbMS layer depth is between 30-45µm. Steam velocity is estimated to be ~200-350 m/s.

Region 2: YbMS layer depth is between 20-30 µm. Steam velocity is estimated to be ~100-200 m/s.

Region 3: YbMS layer depth is between 10-20 µm. Steam velocity is estimated to be ~50-100 m/s.

Region 4: YbMS layer is discontinuous, form between 5-10 µm. Steam velocity is estimated to be ≤ 50 m/s.

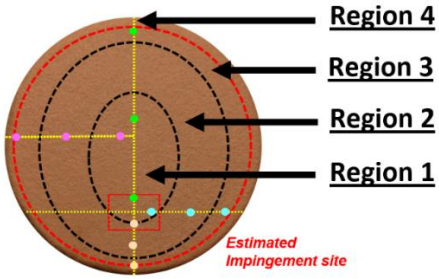

Figure 9: YbMS layer depth of formation profile generated from experimental results based on data averaged at points for steam exposure at t = 96 h, T= 1375 ℃

Following steam jet exposure and cross-sectioning, quantitative image analysis was performed using Fiji in combination with a machine learning-based segmentation and classification approach to determine the percent porosity within the steam-induced YbMS reaction layer as shown in Figure 10 [14].

Representative regions corresponding to each material component were manually labeled and input into the system to guide classifier training. The trained model generated probability maps. From these maps, the porosity regions were isolated by applying a threshold to create a binary mask, which allowed for calculation of the area fraction occupied by pores relative to the selected cross-section.

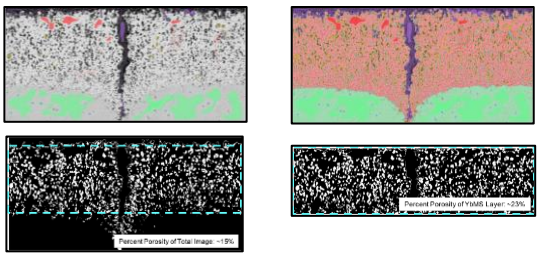

Figure 10: Classifier training and labeling of distinct material components in the coating with cropped region of interest for sintered YbDS percent porosity formation (Steam exposure: t = 96 h, T = 1375 ℃)

Quantitative image analysis of the YbMS reaction layer revealed notable differences in porosity between the sintered and APS YbDS samples as seen in Figure 11.

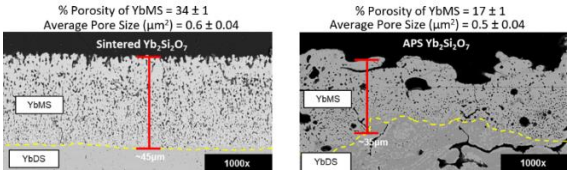

Figure 11: Difference in coating processing between sintered and APS coatings and their impact on percent porosity found in the YbMS layer, and average pore size grown for steam exposure at t = 96 h, T = 1375 ℃

Experimental Setup – Steam + Thermal Gradient

Prior to steam testing, coating surfaces were mechanically polished down to 12.7µm to reduce the surface roughness associated with the APS coating deposition process

To isolate the effects of thermal gradients, two APS YbDS samples were exposed to identical steam conditions (1375 °C for 255 hours). One sample was then exposed to thermal gradient testing at an external location, while the other was retained in the steam-exposed condition for comparison. This approach enables direct evaluation of the role of thermal gradients in driving crack formation in steam-degraded coatings.

Thermal gradient cycling was performed using a cyclic heating and cooling schedule consisting of three minutes of heating followed by two minutes of cooling, for a total of 2000 cycles.

Thermal gradients were generated using a high heat flux CO_2 laser-based testing system. In this setup, the coating surface is rapidly heated, while the backside of the sample is simultaneously cooled using a high-velocity water mist. This combination of localized heating and active cooling produces a steep through-thickness temperature gradient that closely replicates the thermal conditions experienced in service.

Temperature measurements were obtained using non-contact pyrometry and infrared imaging to monitor both the coating surface and substrate temperatures during testing. The imposed thermal gradients generate tensile stresses during cooling promoting crack initiation, propagation, and potential spallation within the coating system.

Results – Steam + Thermal Gradient

Following thermal gradient testing, extensive mud cracking was observed across the YbMS layer compared to the steam-only exposed sample. These mud cracks formed a segmented network characteristic of tensile stress relief across the surface layer. Cracking was most prominent near the steam impingement region, where the YbMS layer was thickest, indicating a strong correlation between reaction layer formation and crack initiation. In these regions, the mud crack network appeared larger, reflecting higher local damage accumulation. Secondary electron imaging using an Everhart-Thornley detector (ETD) on the SEM further revealed localized surface lifting, with charging behavior indicating partial coating delamination, shown in Figure 12.

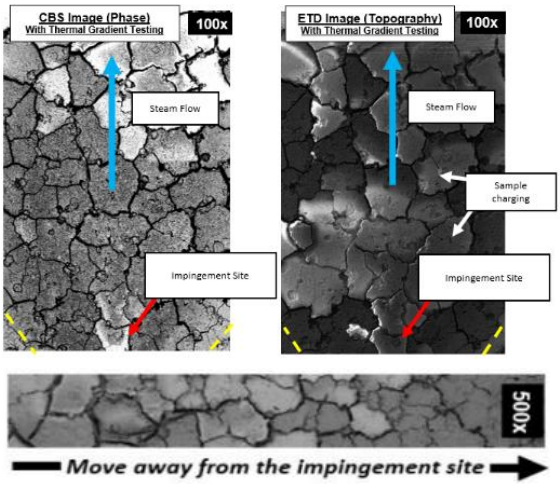

Figure 12: Plan-view SEM backscatter image showing at and above the impingement site where YbMS reaction layer is formed, with ETD demonstrating coating has been raised representing partial spallation. Steam exposure at t = 255 h, T = 1375°C with thermal gradient

As the distance from the impingement site increased, and the YbMS layer thickness decreased, a corresponding reduction in cracking severity was observed. This was characterized by smaller mud crack segment sizes, decreasing an average of 0.14mm, and a reduced spacing between crack segments, decreasing an average of 0.02mm, as shown in Table 2 and Table 3 respectively using Fiji image analysis tool [14]. The smallest spacing that could be reliably measured was 0.01 mm, explaining the standard deviation for the smallest measurements (0.01 mm) appearing as 0.00 mm. These trends indicate a general dependence of crack morphology on both the extent of YbMS formation and the local thermal gradient, confirming that thicker, more degraded regions of the coating are more susceptible to damage.

Table 2: Measured mud crack segment size change within and along the boundary of the steam impingement region using Fiji image analysis tool. t = 255 h, T = 1375°C

Steam + Thermal Gradient	Within Steam Impingement Region	Along boundary of Steam Impingement Region
Average (mm)	0.23	0.09
Std. Deviation (mm)	0.03	0.03

Table 3: Measured spacing between crack segments within and along the boundary of the steam impingement region using Fiji image analysis tool. t = 255 h, T = 1375°C

Steam + Thermal Gradient	Within Steam Impingement Region	Along boundary of Steam Impingement Region
Average (mm)	0.03	0.01
Std. Deviation (mm)	0.01	0.00*

The formation and uniformity of the steam-induced YbMS reaction layer were characterized using SEM imaging of the vertical cross-section.

Both samples exhibited nearly identical YbMS layer thickness profiles as seen in Figure 14, with the maximum depth of approximately 150 µm at the center of the impingement region gradually decreasing to roughly 60 µm near the edges.

Four primary crack types were identified in this study, representing the progressive stages of damage evolution within the coating system [15]. These crack types are distinguished based on their depth of penetration, interaction with interfaces, and their contribution to coating degradation and failure.

1.) YbMS Part-Through Cracking: Cracks are confined within the YbMS reaction layer and do not extend to the underlying interface or YbDS layer.

2.) YbMS Through-Cracking with Partial Delamination: Cracks are confined within the YbMS reaction layer and reach the interface layer

3.) YbMS Through-cracking with YbDS Part-Through Cracking: Cracks penetrate through the interface layer and extend into the underlying YbDS layer, it does not interact or reach the TGO layer.

4.) YbMS Through-cracking with YbDS Through-Cracking with TGO Layer Growth: Cracks penetrate through the interface layer and extend into the underlying YbDS layer, reaching the TGO layer.

From experimental results shown in Figure 14, it is found that under steam-only conditions, damage is predominantly limited to YbMS part-through cracking, where cracks remain confined within the reaction layer and likely serve as a mechanism for localized stress relief. However, the introduction of thermal gradient cycling is shown to increase crack width and lead to bifurcation across the YbMS/YbDS interface.

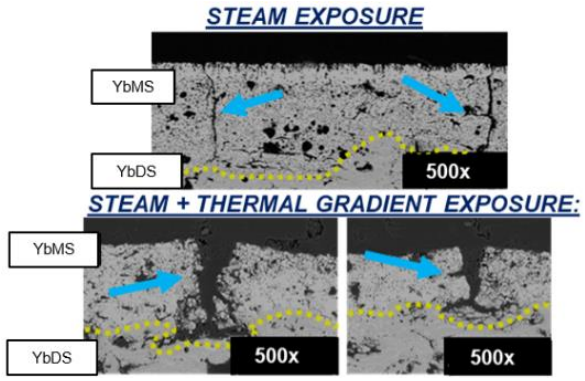

Figure 14: Experimental Results demonstrating steam and steam+thermal gradient exposure crack growth. Steam exposure at t = 255 h, T = 1375 ℃

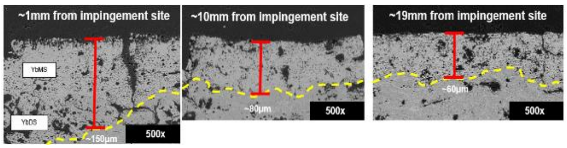

Figure 13: APS YbDS Vertical Cross-Section without Thermal Gradient Cycling (Steam Exposure: t = 255 h, T = 1375 ℃)

Conclusion

This research validates a modified high-temperature, high-velocity steam jet testing system capable of producing large-area steam degradation in YbDS environmental barrier coatings. The improved experimental design expanded the steam-affected region from approximately 5 mm in earlier systems to nearly the full 25.4 mm diameter of the coating sample, while eliminating mechanical erosion caused by incompletely vaporized water droplets. With the ability to reliably generate large steam-degraded regions on coating samples, Studies on investigating the thermomechanical response of these degraded coatings under thermal gradient conditions can be completed.

Preliminary results from this coupled steam and thermal gradient study demonstrate that as the distance from the impingement site increased, and the YbMS layer thickness decreased, there was corresponding reduction in cracking severity as shown by surface mud crack formations. Additionally, under steam-only conditions, YbMS part-through cracking was found to be the primary mechanism for localized stress relief. In addition, adding thermal gradient cycling exposure increased crack width and promoted crack bifurcation across the YbMS/YbDS interface.

Acknowledgements

This work was supported by Rolls-Royce and supervised by program manager Dr. Stephanie Gong. Additional support was provided by the American Ceramics Society.

References

[1] S. Basu and V. Sarin, "Thermal and Environmental Barrier Coatings for Si-Based Ceramics," *Comprehensive Hard Materials*, vol. 2, pp. 469–489, Mar. 2014, doi: 10.1016/B978-0-08-096527-7.00036-2.

[2] R. W. Olesinski and G. J. Abbaschian, "The C−Si (Carbon-Silicon) system," *Bulletin of Alloy Phase Diagrams*, vol. 5, no. 5, pp. 486–489, 1984, doi: 10.1007/BF02872902.

[3] K. N. Lee, D. S. Fox, and N. P. Bansal, "Rare earth silicate environmental barrier coatings for SiC/SiC composites and Si_3N_4 ceramics," *J. Eur. Ceram. Soc.*, vol. 25, no. 10, pp. 1705–1715, 2005, doi: https://doi.org/10.1016/j.jeurceramsoc.2004.12.013.

[4] M. J. Ridley and B. A. Pint, "FWP FEAA149: 'Next Generation Environmental Barrier Coatings,'" United States, Dec. 2023. doi: 10.2172/2439882.

[5] B. T. Richards, K. A. Young, F. de Francqueville, S. Sehr, M. R. Begley, and H. N. G. Wadley, "Response of ytterbium disilicate–silicon environmental barrier coatings to thermal cycling in water vapor," *Acta Mater.*, vol. 106, pp. 1–14, 2016, doi: https://doi.org/10.1016/j.actamat.2015.12.053.

[6] Y.-P. Huang, Z.-Y. Wei, J. Sun, H.-N. Cai, and G.-J. Yang, "Undulating and porous structure tuned surface cracking behavior of $Yb_2Si_2O_7$ environmental barrier coatings under steam cycling," *J. Eur. Ceram. Soc.*, vol. 43, no. 16, pp. 7644–7655, 2023, doi: https://doi.org/10.1016/j.jeurceramsoc.2023.07.031.

[7] M. Ridley and E. Opila, "Thermochemical stability and microstructural evolution of $Yb_2Si_2O_7$ in high-velocity high-temperature water vapor," *J. Eur. Ceram. Soc.*, vol. 41, no. 5, pp. 3141–3149, 2021, doi: https://doi.org/10.1016/j.jeurceramsoc.2020.05.071.

[8] C. Wassgren, "Notes on Thermodynamics, Fluid Mechanics, and Gas Dynamics - CHAPTER 11 Pipe Flows," Mar. 2021, *Purdue University Department of Mechanical Engineering*. [Online]. Available: https://engineering.purdue.edu/~wassgren/teaching/ME30800/NotesAndReading/PipeFlows_Losses_Reading.pdf

[9] "Theory for the High Mach Number Flow Interfaces: Sutherland's Law," 2025, *COMSOL Multiphysics*. [Online]. Available: https://doc.comsol.com/6.4/docserver/#

[10] F. M. White, *Viscous Fluid Flow*. in McGraw-Hill international edition. McGraw-Hill Higher Education, 2006. [Online]. Available: https://books.google.com/books?id=fl6wPwAACAAJ

[11] I. Spitsberg and J. Steibel, "Thermal and Environmental Barrier Coatings for SiC/SiC CMCs in Aircraft Engine Applications*," *Int. J. Appl. Ceram. Technol.*, vol. 1, pp. 291–301, Mar. 2005, doi: 10.1111/j.1744-7402.2004.tb00181.x.

[12] O. N. Favorsky, "JET ENGINE," in *A-to-Z Guide to Thermodynamics, Heat and Mass Transfer, and Fluids Engineering*, Begellhouse, 2011.

[13] S. L. dos Santos e Lucato, O. H. Sudre, and D. B. Marshall, "A Method for Assessing Reactions of Water Vapor with Materials in High-Speed, High-Temperature Flow," *Journal of the American Ceramic Society*, vol. 94, no. s1, pp. s186–s195, 2011, doi: https://doi.org/10.1111/j.1551-2916.2011.04556.x.

[14] J. Schindelin *et al.*, "Fiji: an open-source platform for biological-image analysis," *Nat. Methods*, vol. 9, no. 7, pp. 676–682, 2012, doi: 10.1038/nmeth.2019.

[15] J. W. Hutchinson, "Stresses and failure modes in thin films and multilayers," 1996. [Online]. Available: https://api.semanticscholar.org/CorpusID:11726712